

# Supplementary Materials

## Molecular Inhibition for Selective CO<sub>2</sub> Conversion

Charles E. Creissen,<sup>1</sup> José Guillermo Rivera de la Cruz,<sup>1</sup> Dilan Karapinar,<sup>1</sup> Dario Taverna,<sup>2</sup>  
Moritz W. Schreiber,<sup>3</sup> Marc Fontecave<sup>1\*</sup>

### Affiliations

<sup>1</sup> *Laboratoire de Chimie des Processus Biologiques, CNRS UMR 8229, Collège de France, Paris, France*

<sup>2</sup> *Institut de Minéralogie et de Physique des Milieux Condensés, UMR 7590 CNRS, Sorbonne Universités, UPMC Univ Paris 06, 4 place Jussieu, 75005 Paris, France*

<sup>3</sup> *Total Research and Technology, Refining and Chemicals, Division CO<sub>2</sub> Conversion, Feluy, 7181 Seneffe, Belgium*

\*Corresponding author. Email: marc.fontecave@college-de-france.fr

### Contents

|                                  |         |
|----------------------------------|---------|
| Methods                          | p 2-8   |
| Computational Methods and Models | p 9-11  |
| Supplementary Figures & Notes    | p 12-36 |
| Supplementary Tables             | p 37-42 |
| Supplementary References         | p 43-44 |

## Materials and Methods

### Materials

Copper nanopowder (Sigma-Aldrich, 25 nm), 4-mercaptopyridine (ACROS organics, 96%), thiophenol (Sigma-Aldrich, ≥99%), N,N-dimethylformamide (Carlo Erba, 99.9%), and methanol (Carlo Erba, 99.9%) were used to form thiol-modified Cu nanoparticles. Polytetrafluoroethylene (PTFE) membranes (Sartorius™, 0.45 μm pore size) and Nafion™ (Sigma-Aldrich, 5 wt% in lower aliphatic alcohols and water) were used for electrode preparation. Milli-Q H<sub>2</sub>O and KOH (Sigma-Aldrich, 99.99%) were used for electrochemical experiments. Terephthalic acid (Sigma-Aldrich, 98%), D<sub>2</sub>O (99.9% D), and sodium formate (Sigma-Aldrich, ≥99%) were used for NMR experiments and calibration.

### Physical Characterisation

All SEM images were obtained using a SU-70 Hitachi FEG-SEM. TEM analysis was conducted using a Jeol 2100F microscope equipped with Schottky Field Emission electron gun and an ultra high resolution polar piece. UV-vis absorption spectra were recorded on liquid samples using an Agilent Cary 100 spectrometer. Fourier-Transform Infrared (FT-IR) spectra were recorded using a Shimadzu Prestige 21 Spectrometer. XPS analysis was conducted using a Thermofisher Scientific Nexsa spectrometer equipped with a monochromated Al-K $\alpha$  anode (1486.6 eV) and a dual flood gun (low energy electron and ion). High energy resolution spectral windows of interest were recorded with a 400 μm spot size. The photoelectron detection was performed using a constant analyzer energy (CAE) mode (20 eV pass energy) and a 0.1 eV energy step. All the associated binding energies were corrected with respect to adventitious carbon C<sub>1s</sub> at 284.8 eV. Quantification was performed based on the Cu<sub>2p3/2</sub>, O<sub>1s</sub>, C<sub>1s</sub>, N<sub>1s</sub>, and S<sub>2p</sub> photopeak areas after a Shirley type background subtraction using the Thermofisher Scientific Avantage© software and its “ALTHERM01” library as sensitivity factor collection.

XPS samples were either powder samples deposited on gold or quartz substrates (pre-electrolysis) or obtained from films through removal using carbon tape (post-electrolysis).

### **Nanoparticle modification**

Cu NPs (Sigma, 25 nm) featuring a native oxide layer formed from ambient exposure, were dispersed in N,N-dimethylformamide (DMF) (1 mL) and sonicated for 15 min at 25 °C. A solution containing 4-mercaptopyridine (SPy, 10 mM, DMF) was added under inert conditions to obtain a mixture of 130 nmol mg<sub>Cu</sub><sup>-1</sup>. The suspension was sonicated for 1 h at 25 °C then the particles were washed three times with DMF, twice with MeOH, and dried *in vacuo* for 24 h to form SPy-modified nanoparticles. Thiophenol (SPh) and 2,6-dimethyl-4-mercaptopyridine (DMSPy) modification was conducted using the same method with the same molar ratio of ligand to Cu NPs. Cu<sub>25</sub>-SPy nanoparticles were formed in the same way but all treatment was carried out in a glovebox to avoid exposure of the particles to oxygen.

### **Electrode Preparation**

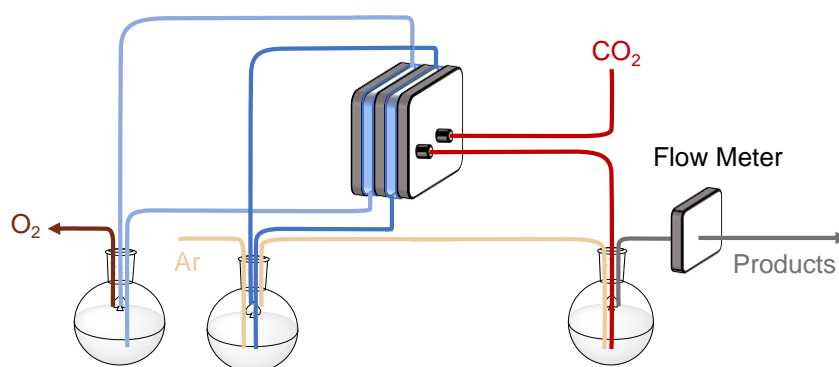
For GDE preparation, an ink containing a weight ratio of 4:3, Cu-SPy:Nafion 5 wt% was prepared in methanol and sonicated for 1 h at 25 °C. The ink was spray deposited onto a PTFE membrane (Sartorius, 0.45 μm pore size) confined to a circular diameter of 2 cm<sup>2</sup> to obtain a total mass loading of approximately 1.75 mg cm<sup>-2</sup> after drying under vacuum. The same mass loading was used for Cu, Cu-SPy, and Cu-SPh electrodes.

### **Electrochemical Experiments**

All electrochemical experiments were conducted with a BioLogic VSP300 or VMP3 potentiostat with a 20 A current booster. Ohmic drop (iR) correction was conducted manually using resistance values obtained using electrochemical impedance spectroscopy.

Electrocatalysis was conducted in a custom-made gas-fed flow cell (Sphere Ltd., see Fig. S1 for diagrams and specific details). An anion exchange membrane (Sustanion, pre-treated in KOH), a Ni-foam anode, and a leak-free Ag/AgCl/KCl<sub>3.4M</sub> reference electrode (Innovative Instruments Ltd.) were used. The PTFE-based GDEs were electrically contacted using Cu tape and confined to a geometric area of 1 cm<sup>2</sup>. Pre-activation was required, which involves consecutive linear sweep voltammograms (LSVs) under CO<sub>2</sub> flow with a sweep rate of 25 mV s<sup>-1</sup> between -0.8 to -1.5 V vs. Ag/AgCl/KCl<sub>3.4M</sub> until stabilisation of the current response. A CO<sub>2</sub> inlet flow rate was maintained at 30 mL min<sup>-1</sup> using a mass flow controller (Bronkhurst) for initial studies and the electrolyte solution (5 M KOH) was circulated at a rate of 5.5 mL min<sup>-1</sup> using a peristaltic pump. The catholyte was constantly purged with Ar at a fixed flow rate of 35 mL min<sup>-1</sup> and the outlet was connected to the CO<sub>2</sub> outlet gas trap in order to carry any liquid saturated gas products to the GC. Additionally, calibrated flow meters (MesaLabs Defender 530+ and Ellutia 7000) were used to verify flow rates before and after the GC inlet to ensure the correct flow value was recorded and to establish the portion of CO<sub>2</sub> utilised to account for mass balance (Scheme 1). The catholyte and anolyte volumes were 20 mL and the electrolysis time was 1 h for all experiments apart from the 6 h electrolysis, where the volumes were increased to 140 mL.

Gas products for CCE experiments were recorded at 20 and 45 minutes to ensure consistent selectivity and liquid products taken after 1 h. For the 6 h electrolysis experiment, liquid samples were extracted using a syringe every 2 h and the gas products recorded every 30 minutes. Potentials were converted to the reversible hydrogen electrode scale (RHE) using the Nernst equation:  $E_{\text{RHE}} = E_{\text{Ag/AgCl/KCl}_{3.4\text{M}}} + 0.206 + 0.0591 \times \text{pH}$  and were iR-corrected to account for the solution resistance, which was obtained from electrochemical impedance spectroscopy scans. Note that this does not account for any local pH changes at the electrode/solution interface, however only small changes are expected for such highly alkaline systems.<sup>1</sup>



**Scheme 1** – Argon is flowed into the catholyte to ensure transfer of all gas products then the CO<sub>2</sub> outlet is fed into the same gas trap as the catholyte gas outlet.

### Gas Product analysis

Gas products were detected on-line using an SRI instruments 8610 GC with Ar as the carrier gas. The GC was fitted with a thermal conductivity detector for H<sub>2</sub> quantification, where the gas was separated using a HaySepD precolumn with a 3 m molecular sieve column. Carbon products were separated using either a 3 m molecular sieve column (CH<sub>4</sub>) or a 5 m HaySepD column (CO, C<sub>2</sub>H<sub>4</sub>, C<sub>2</sub>H<sub>6</sub>) and detected using a flame-ionization detector fitted with a methanizer. Calibration was performed using a custom standard gas mixture in CO<sub>2</sub>.

The FE for gas products was calculated using equation 1:

$$FE (\%) = \frac{n_{\text{product}} \times n_{\text{electrons}} \times F}{(Q_{t=0} - Q_{t=x})} \quad (1)$$

Where  $n_{\text{product}}$  is the amount of product (mol),  $n_{\text{electrons}}$  is the number of electrons used to make the product,  $F$  is the Faraday constant (C mol<sup>-1</sup>),  $Q_{t=0}$  is the charge at the time of the injection, and  $Q_{t=x}$  is the charge at time  $x$  seconds before the injection, representing the time taken to fill the sample loop, with  $x$  depending on the combined flow rate of Ar and CO<sub>2</sub> as well as the loop size.

The full cell energy efficiency  $EE_{\text{full}}$  for formate was calculated using equation 2:

$$EE_{full}(\%) = \sum \frac{FE_{product} \times E_{product}}{E_{cell}} \quad (2)$$

Where  $E_{cell}$  is the measured cell potential,  $FE_{product}$  is the faradaic efficiency (%), and  $E_{product}$  is the thermodynamic potential for formate ( $-0.02$  V). We chose to use the formate standard potential rather than formic acid to avoid over-evaluation of the energy efficiency. For  $EE_{1/2}$  values,  $E_{cell} = E_{1/2} + E_{H_2O/O_2}$ , where  $E_{1/2}$  is the iR-corrected potential measured in the cell (V vs. RHE) and  $E_{H_2O/O_2}$  is 1.23 V.

### Liquid Product Analysis

Liquid products were analysed using  $^1H$  NMR with a presaturation water suppression method on a Bruker Advance III 300 MHz spectrometer at 300 K.  $D_2O$  was used as the lock solvent and an aqueous solution of terephthalic acid used as an internal standard for quantification. Formate values were confirmed with a standard calibration using sodium formate solutions (in 5 M KOH) to ensure accuracy. The crossover of formate through the anion exchange membrane was accounted for by also liquid sampling from the anode compartment. Example spectrum shown in Fig. S10.

### Single-Pass Carbon Efficiency Calculations

Calculations were based on the volumetric flow entering and leaving the cell as well as the consumed flow rates involved in both product generation and reactions with  $OH^-$ . The ideal gas law was used to relate the volumetric flow rate to the molar flow:

$$PQ_f = N_f RT \quad (3)$$

Where P is pressure  $Q_f$  the volumetric flow,  $N_f$  the molar flow, R the gas constant, and T the temperature. The molar flow can be calculated using the molar values of each gas in the loop as long as the time taken to fill the loop is known. In our case the loop has a known size, so the time can be calculated given that we know the flow rate into the GC (equation 4):

$$N_f^{product} = \frac{n_{product}}{time\ to\ fill\ loop} \quad (4)$$

The volumetric flow of products is calculated which represents the additional flow for gasses generated in the CO<sub>2</sub>R reaction (equation 5):

$$Q_f^{product} = N_f^{product} \times RT \quad (5)$$

The difference between the outlet flow and the sum of the product volumetric flow rates is the flow rate of unreacted CO<sub>2</sub> in the system (equation 6):

$$Q_f^{residual} = Q_f^{outlet} - \sum Q_f^{product} \quad (6)$$

From here, the amount of CO<sub>2</sub> (in terms of volumetric flow) consumed by generating gas and liquid products can be calculated using equations 7 and 8:

$$Q_{gas}^{\#} = \sum Q_f^{product} \times carbon\ atoms \quad (7)$$

$$Q_{liquid}^{\#} = \sum \frac{n_{product} \times carbon\ atoms \times RT}{duration\ of\ experiment} \quad (8)$$

This allows a total flow rate for CO<sub>2</sub> converted into carbonate to be determined using the inlet flow and the calculated product-based flow rates (equation 9):

$$Q_f^{carbonate} = Q_f^{inlet} - Q_f^{residual} - Q_{gas}^{\#} - Q_{liquid}^{\#} \quad (9)$$

The single pass carbon efficiency (equation 10) takes into account the CO<sub>2</sub> consumed and utilised as well as the products generated.

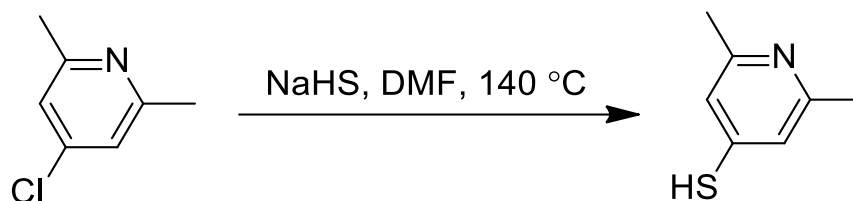
$$\text{Single Pass Carbon Efficiency \%} = \frac{Q_{liq}^{\#} + Q_{gas}^{\#}}{Q_f^{inlet}} \times 100 \quad (10)$$

Calculations were verified using equation 11, which makes use of the partial current density (j) for each carbon product.

$$\text{SPCE \%} = \left[ \left( \frac{j \times 60}{n_{electrons} \times F} \right) \div \left( \frac{\text{flow rate}}{24.05} \right) \right] \times carbon\ atoms \times 100 \quad (11)$$

## Synthesis of 2,6-dimethyl-4-mercaptopyridine

2,6-dimethyl-4-mercaptopyridine (DMSPy) was synthesised according to a previously reported procedure (Scheme 2).<sup>2</sup> Under inert conditions, 2,6-dimethyl-4-chloropyridine (1 g, 7.06 mmol) was dissolved in DMF and NaHS (0.99 g, 17.5 mmol) was added. The mixture was heated to 140 °C for 2 h then concentrated under vacuum. The product was purified using column chromatography (silica, DCM : MeOH = 10 : 1) and dried under vacuum. <sup>1</sup>H NMR (thione tautomer, d<sub>6</sub>-DMSO): δ (ppm) = 6.90 (s, 2H), 2.20 (s, 6H), 12.22 (s, 1H).



**Scheme 2** – Synthesis of 2,6-dimethyl-4-mercaptopyridine (DMSPy)

## Computational methods and models

### Electronic structure calculations

In this study, the Vienna ab initio simulation package (VASP) 5.3.3 was used to perform periodic DFT calculations.<sup>3-6</sup> In order to optimize geometries and calculate electronic energies at 0 K in vacuum, plane-wave basis sets via the projector augmented wave method (PAW) were used to describe the wave function close to the nuclei.<sup>7,8</sup> The wave function was expanded, in terms of plane-wave basis sets with a cut-off energy of 500 eV. Due to the magnetic properties of the system, spin polarization was included. In order to describe long-range interactions, such as van der Waals (vdW) interactions, the DFT-D3 correction method of Grimme *et al.* was applied.<sup>9</sup>

The partial occupancies close to the Fermi level were described by the first-order Methfessel Paxton method which was applied with a smearing width of 0.1 eV. The electronic energy convergence was set to  $1 \times 10^{-6}$  eV. The geometry optimization was carried out until the maximum forces on the atoms were lower than  $1 \times 10^{-2}$  eV  $\text{\AA}^{-1}$  using the Davidson and RMM-DIIS algorithms.<sup>10</sup> These convergence criteria were set as reported on previous studies on Cu.<sup>11-13</sup>

Exchange and correlation energies were calculated using the Revision of the Perdew-Burke-Ernzerhof functional proposed by Hammer *et al.* (RPBE).<sup>14</sup> This functional has shown reliable results in previous studies on the CO<sub>2</sub> reduction reaction (CO<sub>2</sub>RR) over Cu.<sup>11-13</sup> As previously reported, the RPBE functional exhibits systematic deviations on the electronic energies of different gas phase species (H<sub>2</sub>, H<sub>2</sub>O, CO and CO<sub>2</sub>) from the experimental data, hence several corrections for the electronic energies were included to compensate these deviations.<sup>13,15,16</sup> Furthermore, since periodic DFT provides a large deviation in the calculation of gas phase formate (COO<sup>-</sup>) due to its negative net charge, formic acid (HCOOH) was considered as the final product in this study instead of formate, in agreement with previous studies.<sup>17,18</sup>

The catalyst were simulated by repeating the unit cell in three directions to create a periodic

surface slab model. Brillouin-zone integration for the catalyst was performed on a  $5 \times 5 \times 1$  Monkhorst-Pack grid.<sup>19</sup> Gas phase calculations were carried out in a  $20 \text{ \AA} \times 20 \text{ \AA} \times 20 \text{ \AA}$  unit cell considering only the  $\gamma$  point. In order to avoid interactions between periodic images, a vacuum layer of  $20 \text{ \AA}$  was included in the axial direction, coupled with an artificial dipole layer.<sup>20</sup> The electrolyte was incorporated implicitly with the Poisson-Boltzmann model implemented in VASPsol.<sup>21–23</sup> Here, it was considered an electrolyte that consist of an aqueous solution of monovalent anions and cations, the relative permeativity of the media, at room temperature amounts to  $\epsilon_r = 78.4$ , corresponding to water; the concentration of the electrolyte was set to  $5.0 \text{ M}$ , equivalent to a Debye length of  $1.36 \text{ \AA}$ . These settings are intended to mimic typical reaction conditions.<sup>12,13</sup>

The predominant surface, Cu (111) (Fig. S11), was modelled by p(2x2) slab of 4 layers of 16 Cu atoms, where the 2 top layers were allowed to relax and the 2 bottom layers were fixed at their optimal bulk positions.

The structures of adsorbed  $\text{CO}_2^-$  on the Cu and the Cu-SPy surfaces were obtained by removing an H atom from the previously optimized  $^*\text{COOH}$ ,  $^*\text{OCOH}$  and  $^*\text{OCOH}'$  species, and performing a single point calculation, see Figs. S17-S19, this methodology has shown its capabilities to reproduce experimental observations.<sup>24</sup> The main use of this methodology is to overcome the lack of stability of  $\text{CO}_2^-$  which desorbs upon relaxation. A Bader charge analysis was performed and it was found that the non-metallic part ( $\text{CO}_2$ ) gains between 0.60 and 0.70 electrons from the surface (in all the cases), which under reductive potentials (actual reaction conditions) would stabilise these structures.

### **Reaction entropy and enthalpy calculations**

Vibrational frequencies of the adsorbates were calculated for the optimized structures in the presence of the electrolyte to obtain thermal corrections and zero point energies at  $298.15 \text{ K}$ . Frequencies were calculated in the harmonic oscillator approximation, which is described by a

second order expansion of the potential energy surface around the stationary point. The numerical evaluation of the Hessian matrix was performed in VASP, using finite differences, where the selected atoms were displaced 0.015 Å along each Cartesian coordinate. Due to computational restrictions, the vibrational analysis was performed as a partial Hessian analysis in which only the adsorbate and the SPy molecule were allowed to vibrate. Unusually low vibrational modes ( $<50 \text{ cm}^{-1}$ ) were reset to  $50 \text{ cm}^{-1}$ . This protocol provides consistency with previous works.<sup>12,13</sup>

The free energy diagrams for all the electrochemical elementary steps were constructed according to the Computational Hydrogen electrode method (CHE).<sup>11,13,16,25–29</sup> In this approach, the reaction:  $\text{H}^+ + \text{e}^- \rightarrow 1/2 \text{H}_2$  is defined to be in equilibrium at zero voltage, at any given values of pH, at all temperatures, and with at 101325 Pa pressure. Hence, the chemical potential of a proton-electron pair,  $\mu_{\text{H}^+} + \mu_{\text{e}^-}$  can be calculated as half of the chemical potential of gaseous hydrogen ( $1/2 \mu_{\text{H}_2}$ ) at a potential of 0 V. To adjust the chemical potential of the proton-electron pair as a function of the applied potential the following relation is employed  $\Delta G = -eU_{\text{RHE}}$ , where  $e$  is the elementary positive charge and  $U_{\text{RHE}}$  is the applied bias potential.

## Supplementary Figures

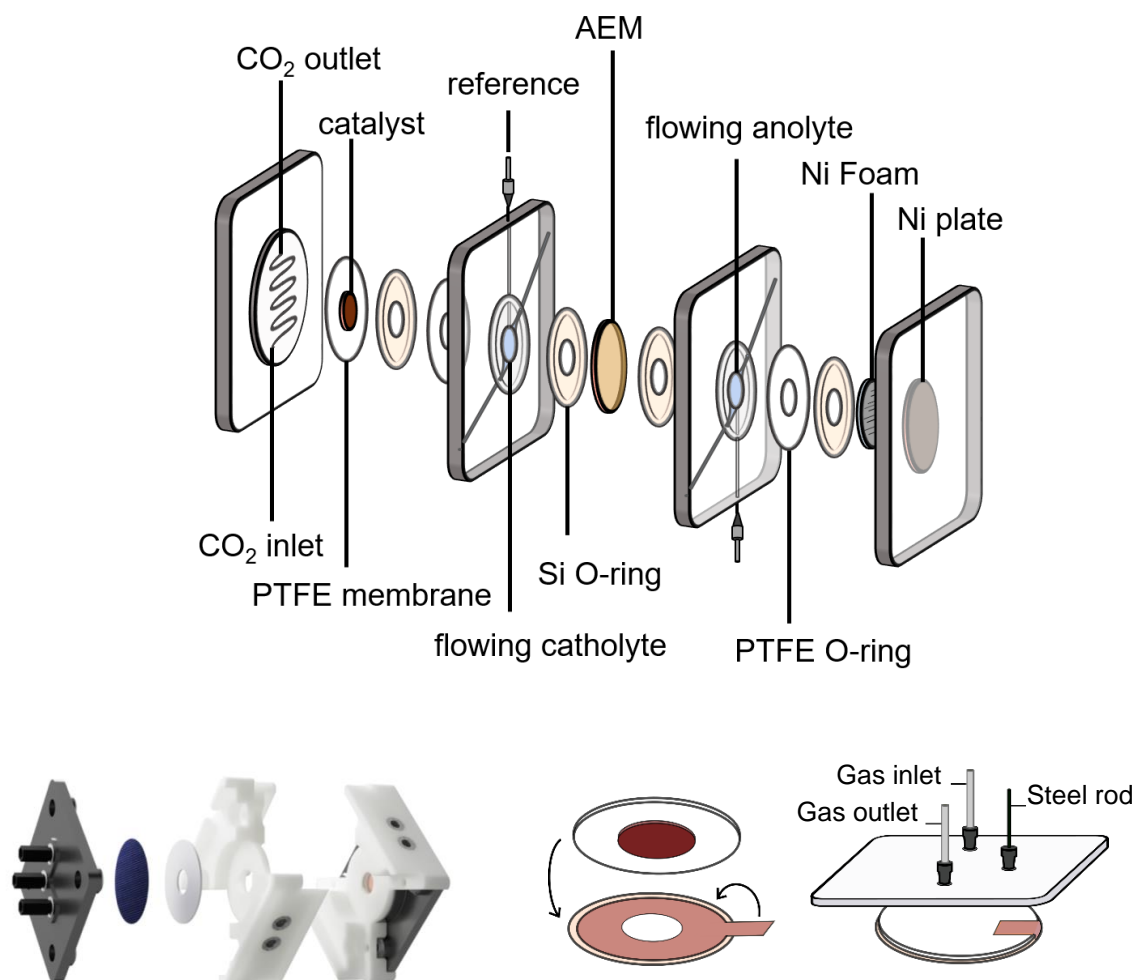


**Fig. S1 | Gas-fed flow cell setup.** Full cell configuration for the gas-fed flow cell (Sphere Energy Corp.). The reference electrodes are leak-free Ag/AgCl/KCl<sub>3.4M</sub> (Innovative Instruments) and AEM represents the anion exchange membrane used for all experiments. The electrolyte was flowed through each compartment from separate containers using a peristaltic pump and the gas fed through the inlet using a mass flow controller. A circular ring of copper tape was used to connect the catalyst to the potentiostat and connection was made through a stainless steel rod from the back of the gas plate as shown.

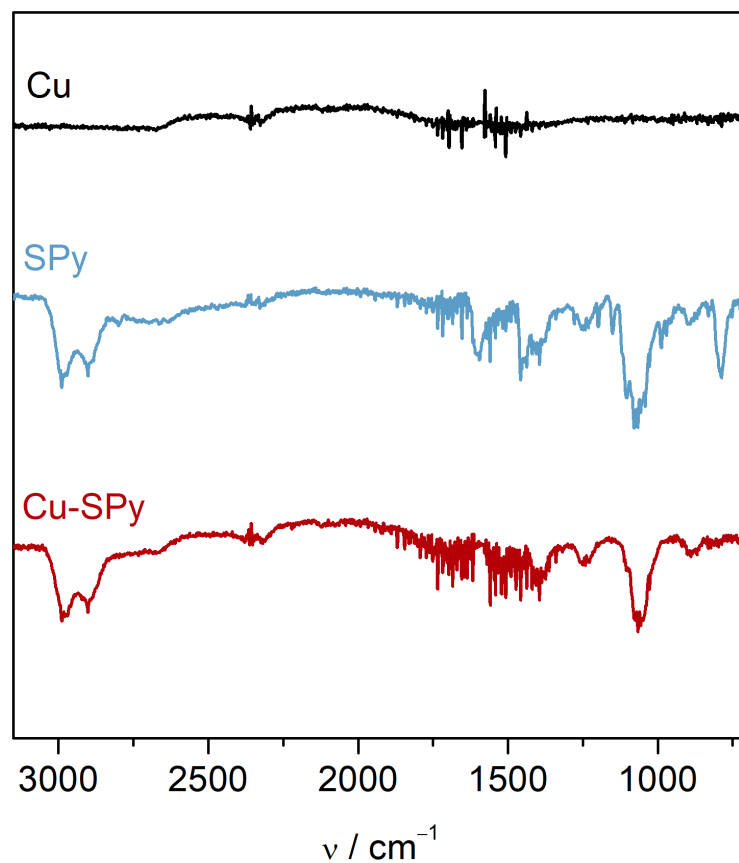


**Fig. S2 | Fourier-Transform Infrared (FTIR) spectroscopy.** FTIR spectra of the bare Cu nanoparticles (black), the SPy ligand (blue), and Cu-SPy nanoparticles (red).

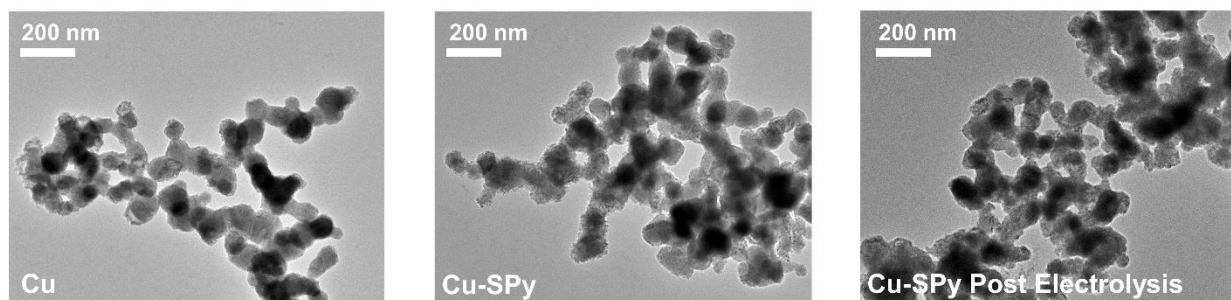


**Fig. S3 | Transmission electron microscopy.** Images of initial Cu-based NPs, as-prepared Cu-SPy, and Cu-SPy NPs following 1 h electrolysis at  $-300 \text{ mA cm}^{-2}$ . No obvious changes in size or morphology were observed before and after modification with SPy. Additionally, there are no clear differences between pre- and post-electrolysis samples suggesting that under these conditions the morphology changes are minimal.

## Note S1 | UV-Vis loading quantification

### Geometric Loading

For geometric molecular loading, ligand stripping was conducted at  $-2.2$  V vs. Ag/AgCl/KCl<sub>3.4M</sub> under Ar flow for 1 h to ensure that all of the molecule was removed (more negative potentials did not give rise to more ligand removal). Samples were taken prior to removal of the applied potential to ensure that no ligand re-adsorption occurred within the cell. Under Ar flow, the desorption of SPy forms 4,4'-dithiodipyridine with an absorption peak at 283 nm in KOH. The absorption peak for desorbed molecule was correlated with a calibration curve for the complex to obtain a molar loading of SPy based on the geometrical area ( $1\text{ cm}^2$ ). The SPy loading value obtained was  $14.6 \pm 2.4\text{ nmol cm}^{-2}$  from 7 electrodes.

### Desorption Under CO<sub>2</sub>R Conditions

Under CO<sub>2</sub> flow, the desorbed thiolate reacts to form a new species with an altered UV-Vis spectrum with a peak at 258 nm – this corresponds to a thiocarbonate species, which have previously been shown to form in reactions of thiolate anions with CO<sub>2</sub>.<sup>30</sup> Through ligand stripping under CO<sub>2</sub> flow for a blank electrode ( $-2.2$  V vs. Ag/AgCl/KCl<sub>3.4M</sub>), and comparison with the absorption peak at 258 nm, an approximate percentage of desorbed species could be obtained. Additional tests were used to show that flow conditions with no applied potential as well the catalyst activation step resulted in loss of ligand (this accounts for the lower signal observed in XPS spectra post-electrolysis) but this stabilised as no additional losses were observed for longer durations of electrolysis at  $-300\text{ mA cm}^{-2}$  (Table S2). It is likely that the physisorbed (thiol) component is more easily lost from the surface whereas the chemisorbed (thiolate) is retained until more negative applied potentials.<sup>31</sup>

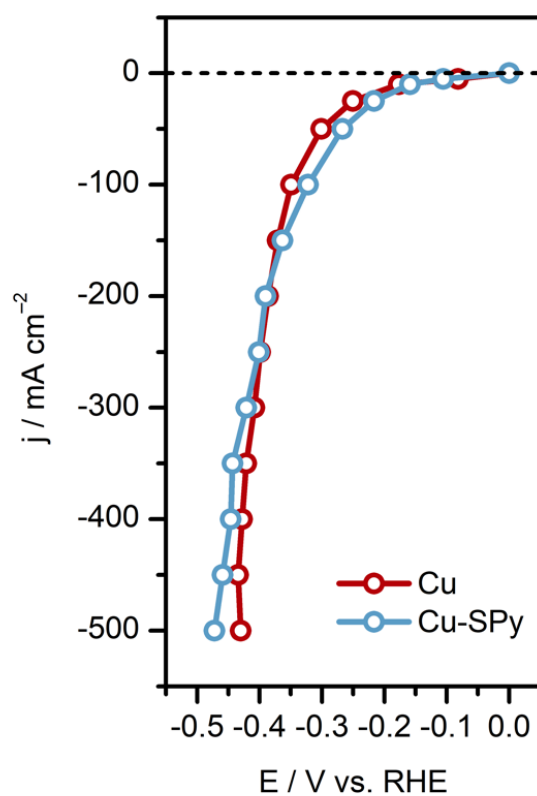


**Fig. S4 | Current-voltage response of Cu and Cu-SPy GDEs.** iR-corrected current-voltage response obtained from chronopotentiometric steps comparing Cu and Cu-SPy electrodes. No clear difference in response could be observed between these two electrodes.

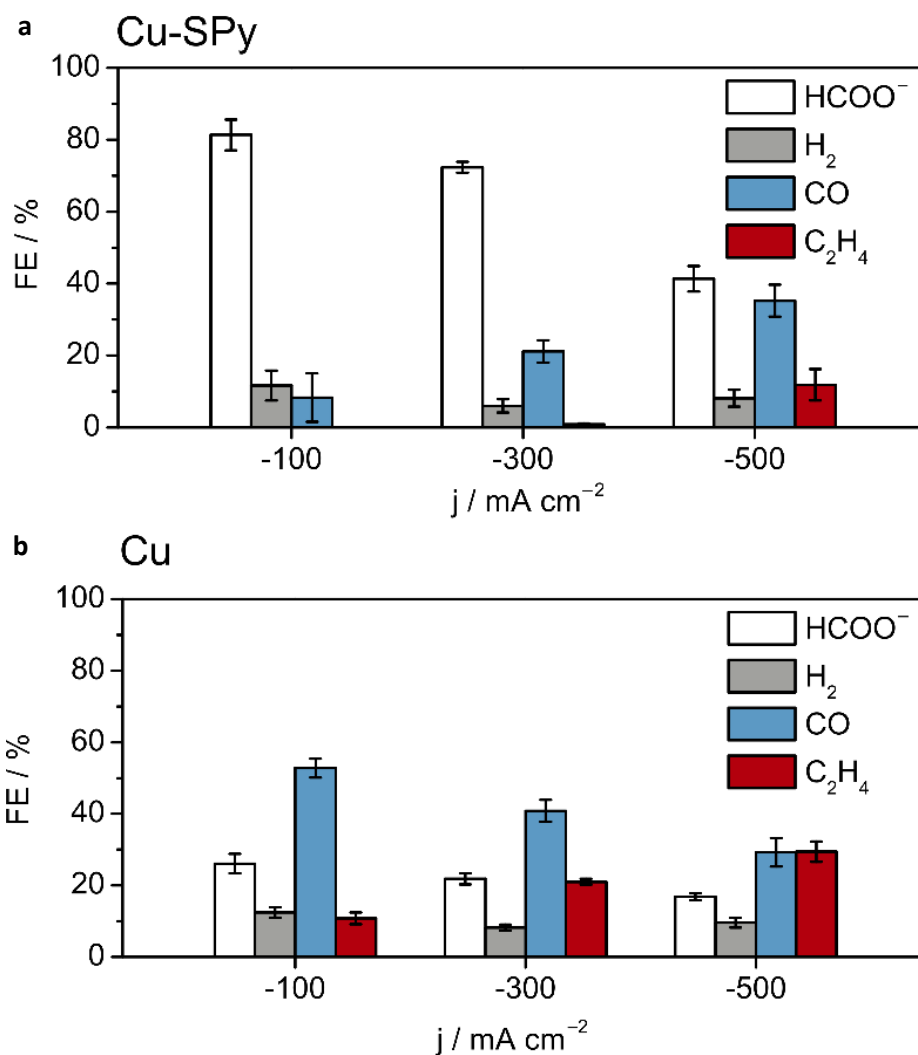


**Fig. S5 | Product distributions for Cu and Cu-SPy GDEs.** Faradaic efficiency (FE) of major products (**a, c**) and partial current densities (**b, d**) from controlled current electrolysis (1h) at different current densities for Cu-SPy and Cu GDEs. Triplicate data obtained with separate electrodes for each point and error bars represent standard deviation from the mean. Gas products obtained from GC injection at 45 minutes and liquid products from anode and cathode compartments were recorded using NMR after 1h. Conditions 5 M KOH, 30 mL min<sup>-1</sup> CO<sub>2</sub> flow, 5.5 mL min<sup>-1</sup> electrolyte solution flow, anolyte and catholyte volume of 20 mL each, geometric electrode area of 1 cm<sup>2</sup>.

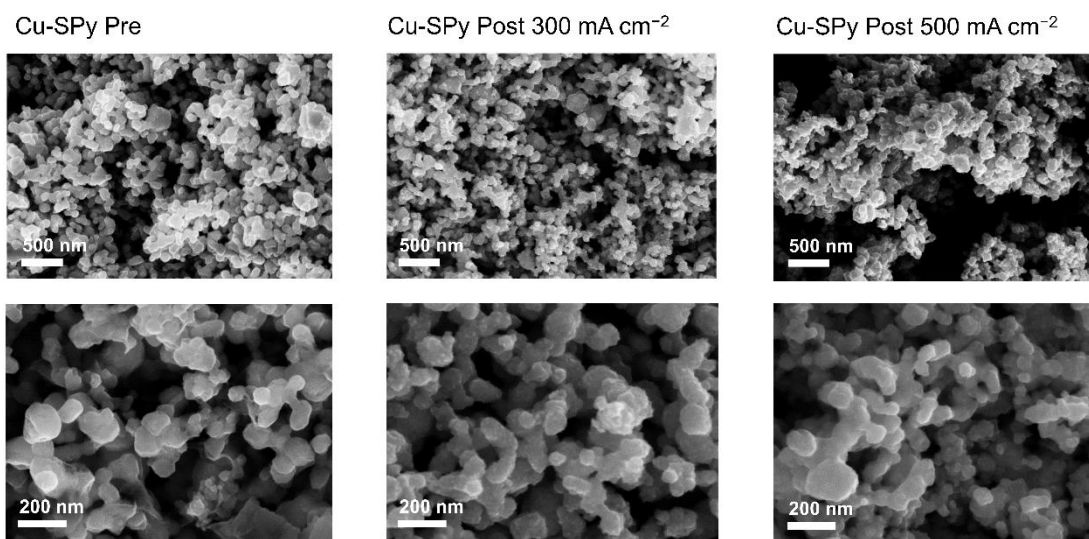


**Fig. S6 | Scanning electron microscopy.** Images of Cu-SPy GDEs before and after electrolysis at different current densities. No significant morphological changes were observed suggesting ligand desorption is not due to surface restructuring.

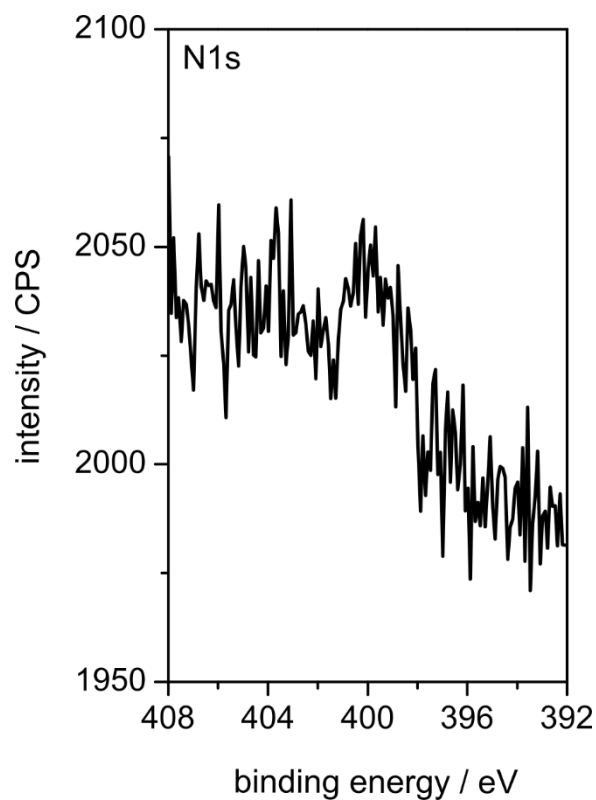


**Fig. S7 | Post-electrolysis XPS.** N<sub>1s</sub> region confirming the presence of SPy after electrolysis at  $-300 \text{ mA cm}^{-2}$  for 1 h. Validation through the sulfur response was not possible due to interference from the S-containing ionomer. The diminished signal compared to the fresh sample is related to ligand loss due to mechanical stripping in the flow cell and activation steps (Table S3).

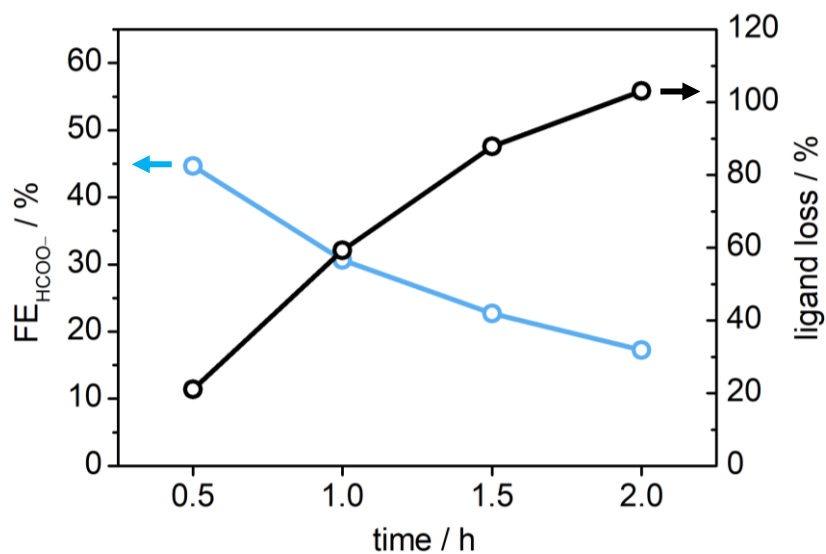


**Fig. S8 | Time-dependent ligand desorption at  $-500 \text{ mA cm}^{-2}$ .** The correlation between  $\text{FE}_{\text{HCOO}^-}$  and the percentage of SPy ligand lost to solution as determined by UV-Vis from an electrode held at  $-500 \text{ mA cm}^{-2}$  over the course of 2 h. The relative percentage was obtained by comparison of the UV-vis peak at 258 nm for an electrode where the ligand was completely removed under  $\text{CO}_2\text{R}$  conditions. The  $\text{FE}_{\text{HCOO}^-}$  of a bare Cu GDE was recovered after 2 h showing that the permanent effects of molecule desorption are minimal and highlighting the key role of the SPy ligand in directing selectivity towards formate.

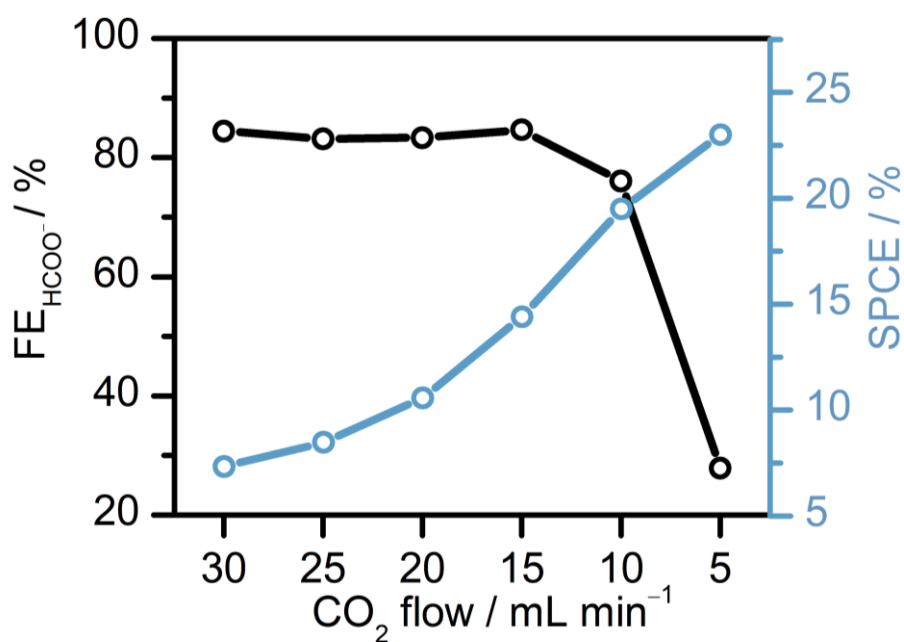


**Fig. S9 | Single-pass conversion efficiency with varying CO<sub>2</sub> flow rate.** The optimum flow rate that doesn't affect FE<sub>HCOO<sup>-</sup></sub> is 15 mL min<sup>-1</sup>. Each point was determined from 30-minute electrolysis at  $-300 \text{ mA cm}^{-2}$  with fresh electrolyte solution. Conditions: 5 M KOH, 5.5 mL min<sup>-1</sup> electrolyte solution flow, anolyte and catholyte volume of 20 mL each, geometric electrode area of 1 cm<sup>2</sup>.

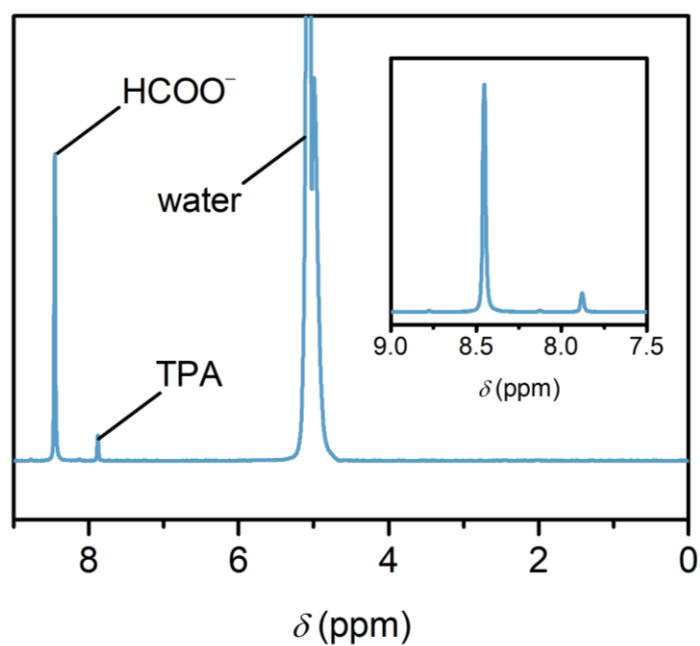


**Fig. S10 | Representative  $^1\text{H-NMR}$  spectrum.**  $^1\text{H-NMR}$  spectrum of the catholyte for a Cu-SPy electrode following electrolysis. TPA = terephthalic acid. A calibration curve for formate was used to ensure accuracy and sampling from the anode compartment was required to account for full amounts of liquid products seeing as product crossover occurred through the anion exchange membrane.

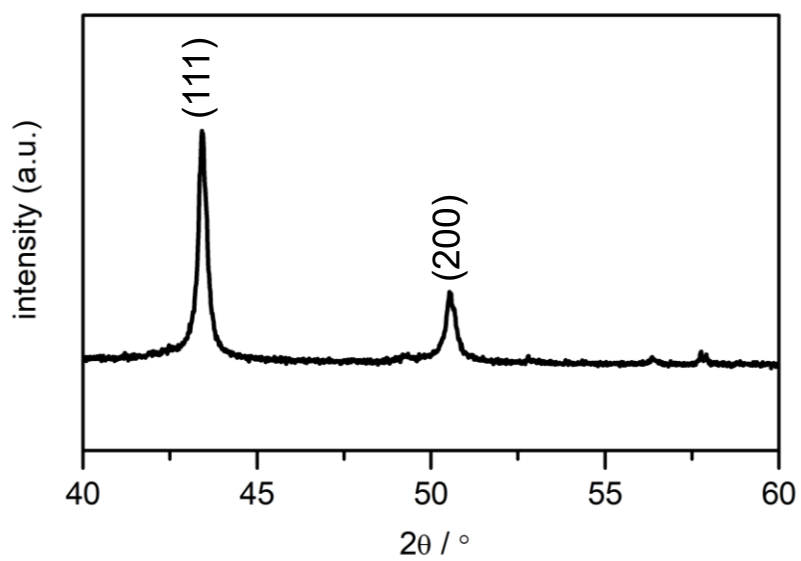


**Fig. S11 | XRD of Cu-SPy sample post-electrolysis at  $-300 \text{ mA cm}^{-2}$ .**

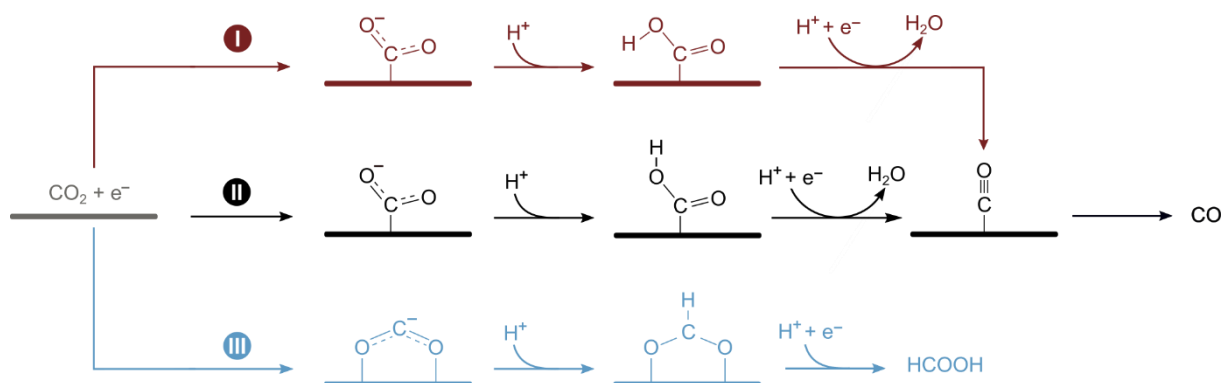


**Fig. S12 | Reaction mechanisms for  $\text{CO}_2$  reduction on Cu and Cu-SPy.** Paths I and II lead to CO whereas path III gives formate. The mechanism involving  $\text{CO}_2$  adsorption with subsequent proton coupled electron transfers was selected. A  $\text{CO}_2$  molecule from the homogeneous phase is first reduced by one electron, producing 3 different chemisorbed surface species. These undergo proton addition to obtain the first PCET species:  $^*\text{OCOH}$ ,  $^*\text{OCOH}'$ , and  $^*\text{COOH}$ .

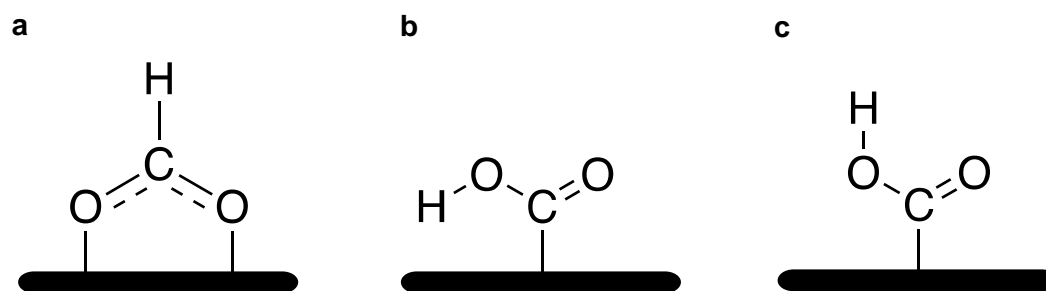


**Fig. S13 | Stable configurations of first PCET intermediates.** Schematic 2D representations of the three most stable adsorbed species. **a**  $^*\text{COOH}$ , **b**  $^*\text{OCOH}$ , and **c**  $^*\text{OCOH}'$ . The calculated electronic adsorption energies for the most stable configurations are reported in Table S4.

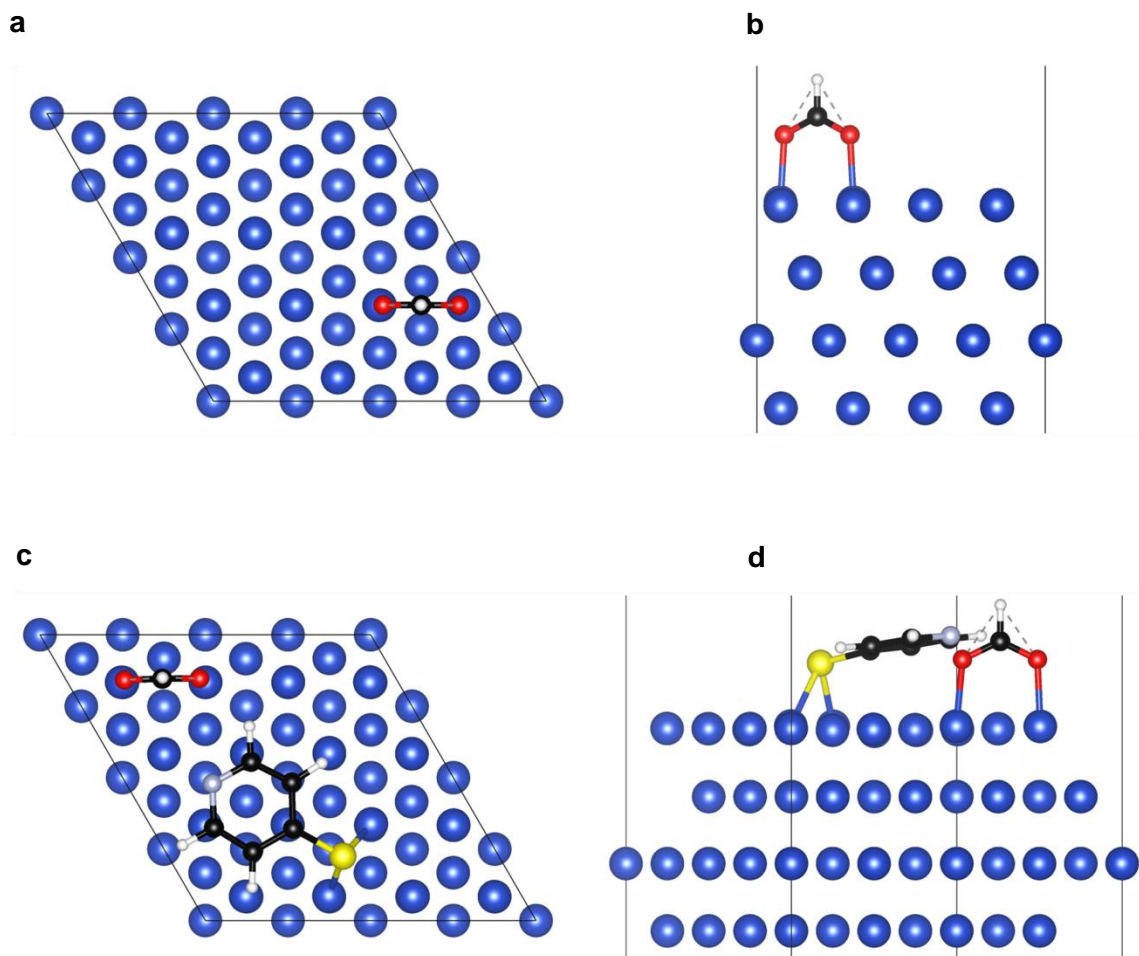


**Fig. S14 |  $^*COOH$  on Cu and Cu-SPy.** The most stable configuration of the adsorbed formate ( $^*COOH$ ) on Cu (**a**, **b**) and Cu-SPy (**c**, **d**). There are no structural changes between  $^*COOH$  species adsorbed on Cu and Cu-SPy. However, Cu-SPy shows a marginally decreased adsorption energy ( $-0.17$  eV) when compared with clean Cu. Colour code: black = carbon, white = hydrogen, grey = nitrogen, yellow = sulfur, blue = copper.

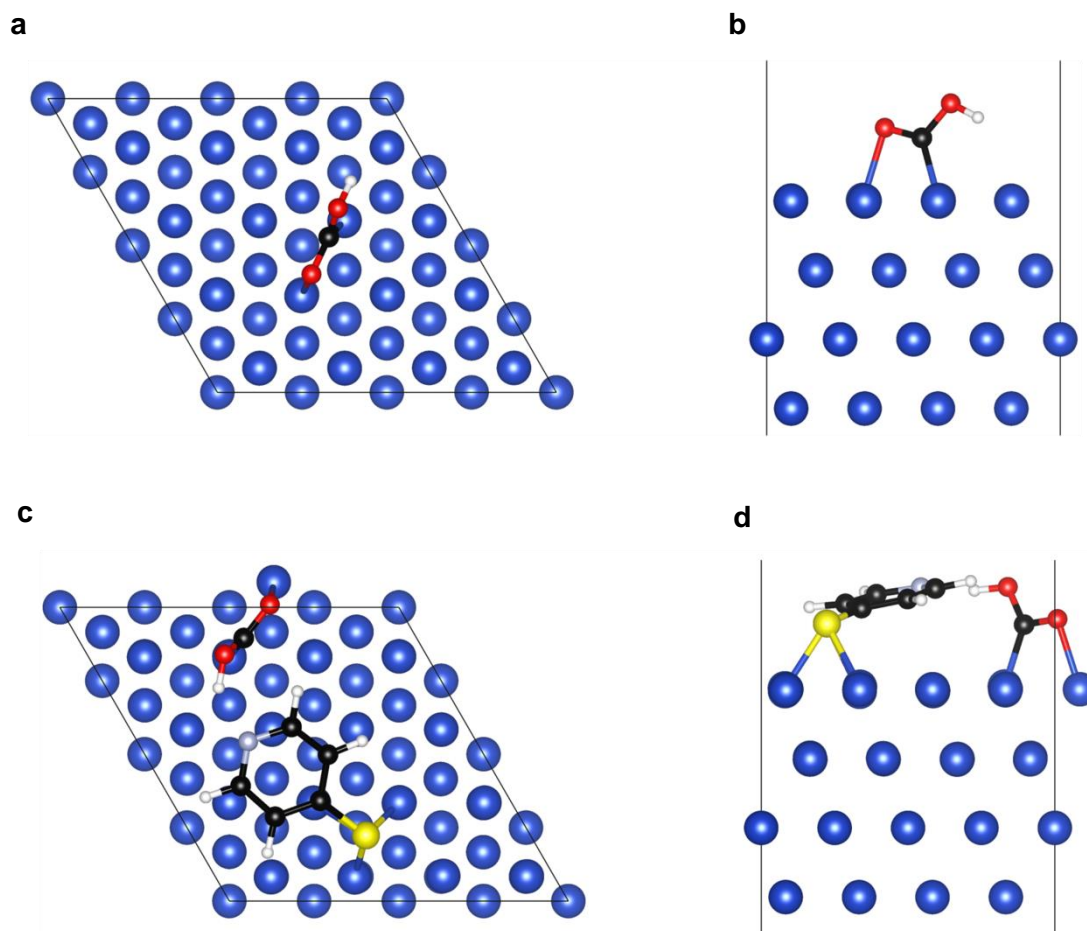


**Fig. S15 | \*OCOH on Cu and Cu-SPy.** The most stable configuration of the adsorbed \*OCOH on Cu (**a, b**) and Cu-SPy (**c, d**). Structural changes between Cu, where the \*OCOH remains adsorbed perpendicular to the surface (dihedral angle O-C-O-H amounts to  $180^\circ$ ), and Cu-SPy surface where one O atom is slightly tilted in away from the N atom of the SPy molecule. The O-H is tilted towards the N atom of the adsorbed SPy molecule leading to a dihedral angle O-C-O-H of  $150^\circ$ . Colour code: black = carbon, white = hydrogen, grey = nitrogen, yellow = sulfur, blue = copper.

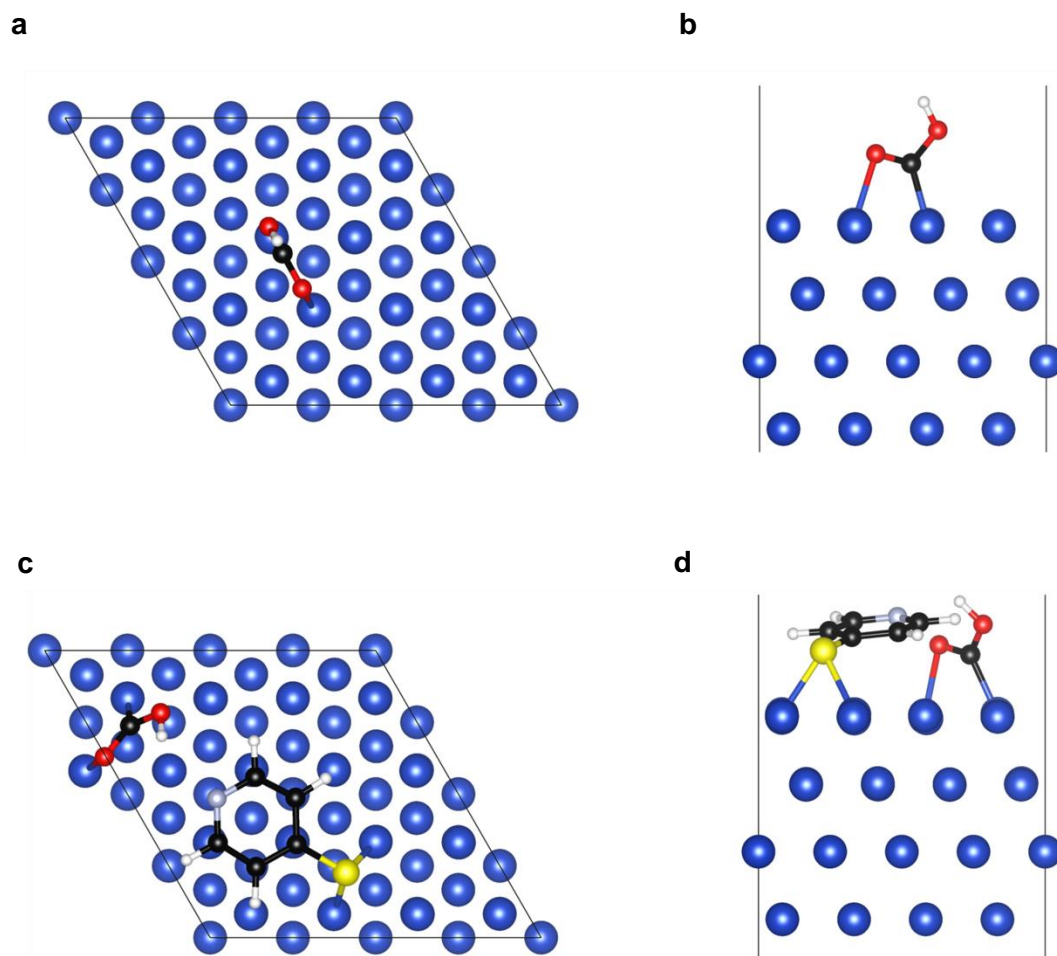


**Fig. S16 |  $*\text{OCOH}'$  on Cu and Cu-SPy.** The most stable configuration of the adsorbed  $*\text{OCOH}'$  on Cu (a, b) and Cu-SPy (c, d). For both the clean Cu and the Cu-SPy surface, the  $*\text{OCOH}'$  species remains adsorbed perpendicular to the surface via a C and an O atom in a rather bridge configuration, with all the molecule atoms in the same plane (dihedral angle O-C-O-H amounts to  $179^\circ$ ). The  $*\text{OCOH}'$  species preserve the same structure with negligible modifications when it is adsorbed on the modified Cu-SPy surface with only a minor increment of 0.15 eV calculated when the  $*\text{OCOH}'$  is adsorbed on Cu-SPy. Colour code: black = carbon, white = hydrogen, grey = nitrogen, yellow = sulfur, blue = copper.

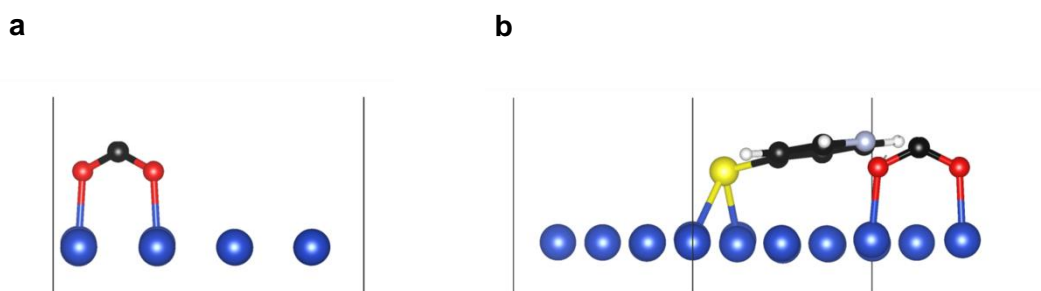


**Fig. S17 |  $\text{CO}_2^-$  adsorbed structures from  $^*\text{COOH}$  on Cu and Cu-SPy.** Schematic representation of the most stable adsorption configuration of  $^*\text{CO}_2^-$  (from  $^*\text{COOH}$ ) on Cu (**a**) and Cu-SPy (**b**). Colour code: black = carbon, white = hydrogen, grey = nitrogen, yellow = sulfur, blue = copper.

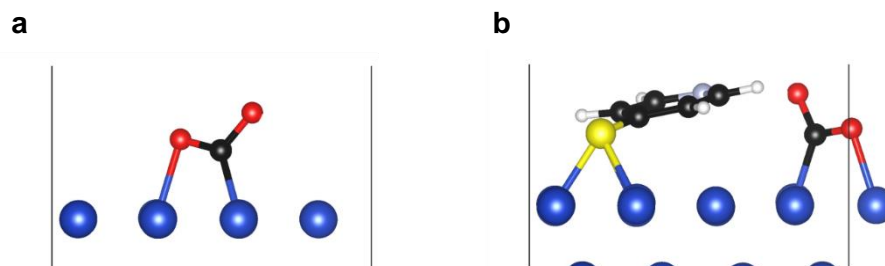


**Fig. S18 |  $\text{CO}_2^-$  adsorbed structures from  $^*\text{OCOH}$  on Cu and Cu-SPy.** Schematic representation of the most stable adsorption configuration of  $^*\text{CO}_2^-$  on Cu (**a**) and Cu-SPy (**b**). Colour code: black = carbon, white = hydrogen, grey = nitrogen, yellow = sulfur, blue = copper.

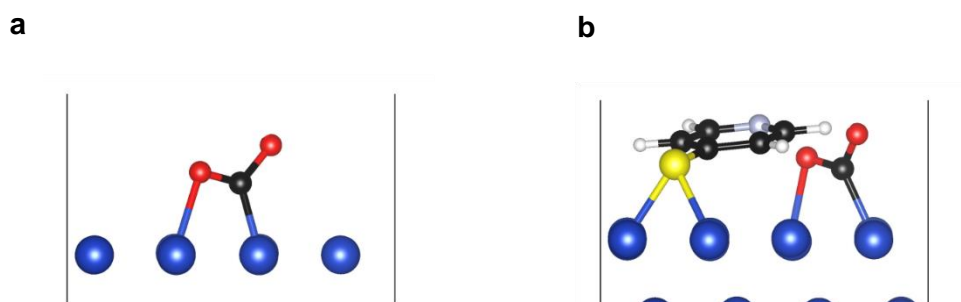


**Fig. S19 | CO<sub>2</sub><sup>-</sup> adsorbed structures from \*OCOH' on Cu and Cu-SPy.** Schematic representation of the most stable adsorption configuration of \*CO<sub>2</sub><sup>-</sup> on Cu (**a**) and Cu-SPy (**b**). Colour code: black = carbon, white = hydrogen, grey = nitrogen, yellow = sulfur, blue = copper

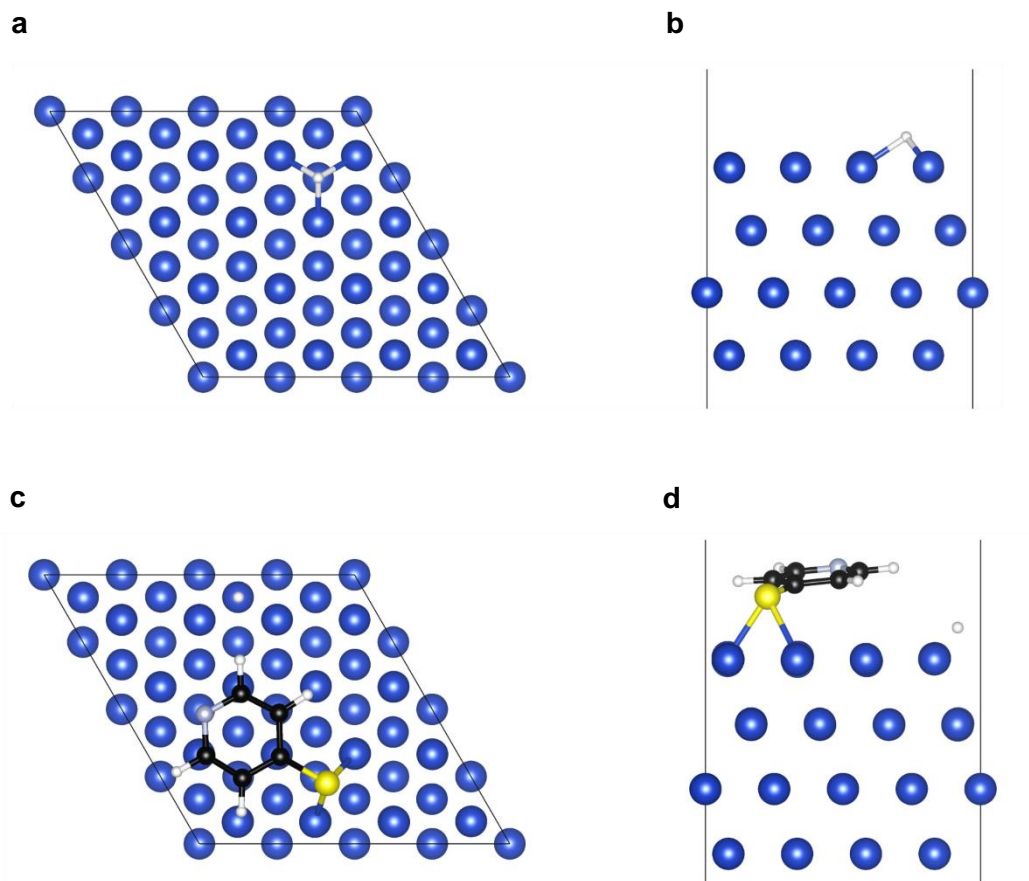


**Fig. S20 | Adsorbed \*H on Cu and Cu-SPy.** Schematic representation of the most stable adsorption configurations of H adsorbed on Cu (**a, b**) and Cu-SPy (**c, d**).

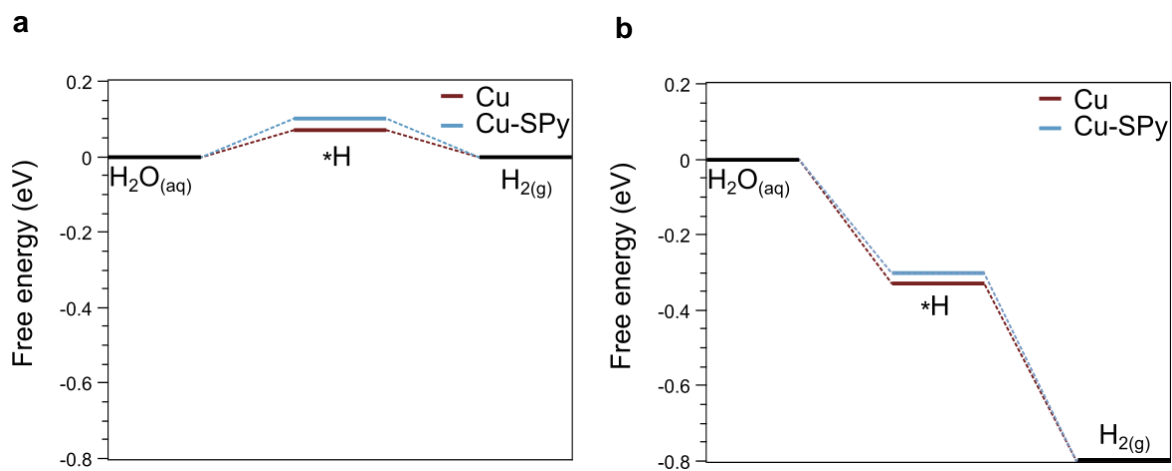


**Fig. S21 | Reaction free energy profiles for hydrogen evolution.** Reaction profiles at **a**, 0.0 V vs. RHE, and **b**, -0.4 V vs. RHE for Cu and Cu-SPy surfaces showing minimal differences with and without the molecular modification.

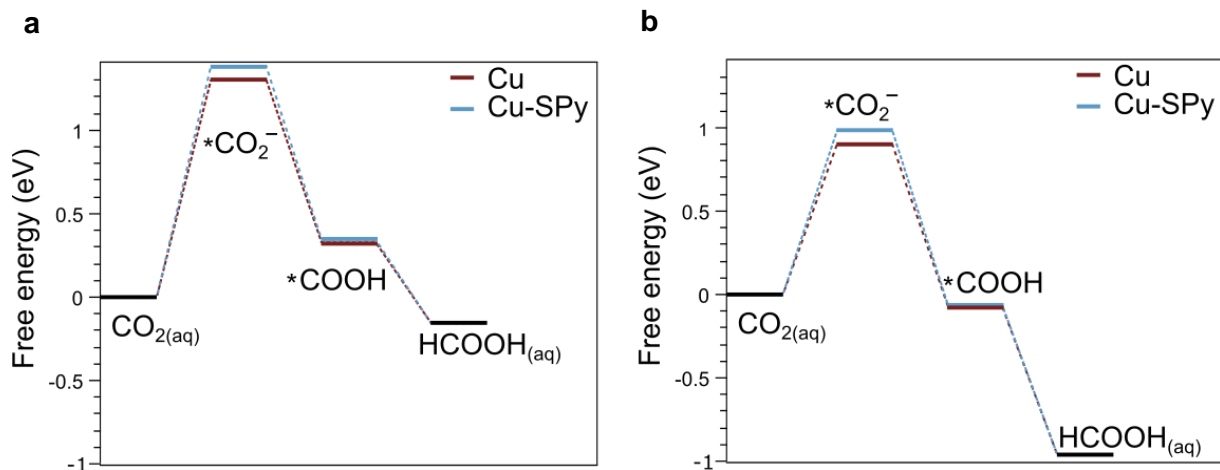


**Fig. S22 | Reaction free energy profiles for formate evolution.** Reaction profiles at **a**, 0.0 V vs. RHE, and **b**, -0.4 V vs. RHE for Cu and Cu-SPy surfaces showing minimal differences with and without the molecular modification.

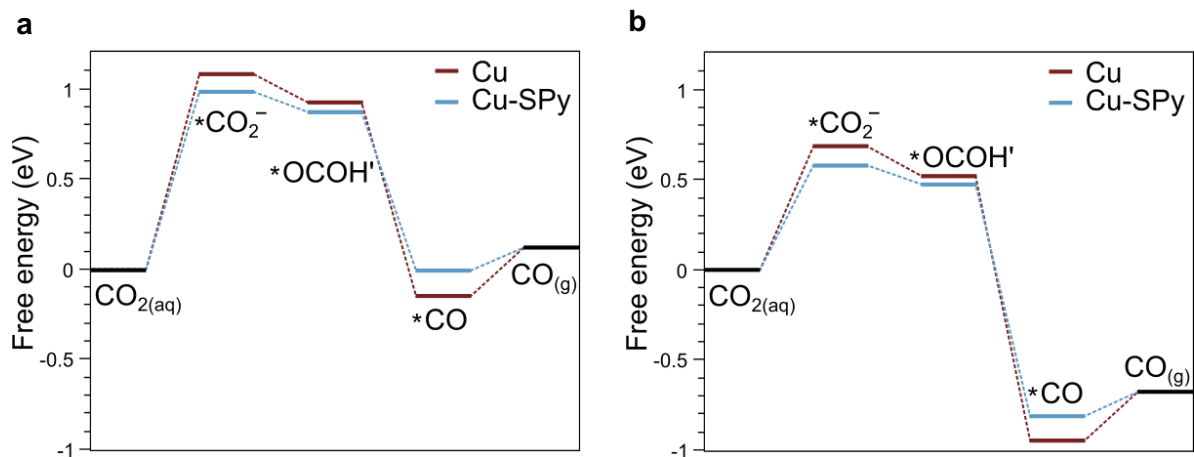


**Fig. S23 | Reaction free energy profiles for CO evolution following the  $*\text{OCOH}'$  pathway.**

Reaction profiles at **a**, 0.0 V vs. RHE, and **b**, -0.4 V vs. RHE for Cu and Cu-SPy surfaces showing minimal differences with and without the molecular modification for this specific CO pathway.

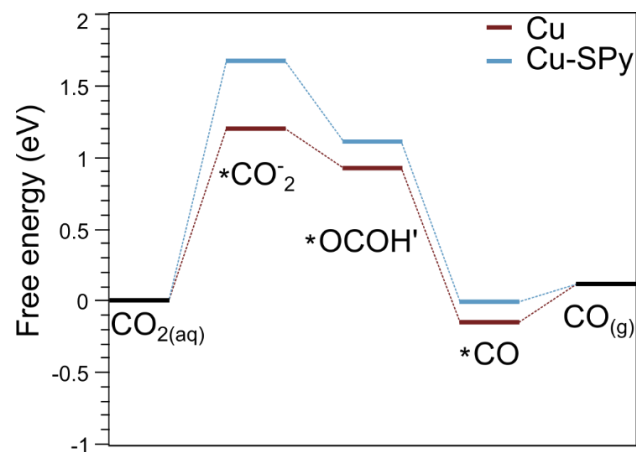


**Fig. S24 | Reaction free energy profiles for CO evolution following the  $^*\text{OCOH}'$  pathway.**

Reaction profiles at 0.0 V vs. RHE for Cu and Cu-SPy surfaces showing significant differences with the molecular modification for this specific CO pathway.

## Supplementary Tables

**Table S1** | XPS analysis of Cu-SPy

| Element (orbital) | Atomic / % | Binding Energy / eV | Atomic / % |
|-------------------|------------|---------------------|------------|
| <b>N(1s)</b>      | 2.03       | 399.0               | 0.81       |
|                   |            | 399.8               | 1.06       |
|                   |            | 401.2               | 0.16       |
| <b>S(2p)</b>      | 1.73       | 163.1               | 1.27       |
|                   |            | 164.3               | -          |
|                   |            | 168.2               | 0.46       |
|                   |            | 169.4               | -          |
| <b>C(1s)</b>      | 26.4       | 285.2               | 26.4       |
| <b>Cu(2p)</b>     | 17.5       | 933.6               | 17.5       |
| <b>O(1s)</b>      | 52.3       | 533.0               | 52.3       |

**Table S2** | Cu-SPy, and Cu faradaic efficiencies of main products from CO<sub>2</sub> reduction (1h) at different current densities with corresponding average half-cell voltages and energy efficiencies for HCOO<sup>-</sup>

| j / mA<br>cm <sup>-2</sup> | E / V vs.<br>RHE (-iR) | Faradaic Efficiency / % |            |                   |                               |           |           |           |             |                                    |
|----------------------------|------------------------|-------------------------|------------|-------------------|-------------------------------|-----------|-----------|-----------|-------------|------------------------------------|
|                            |                        | H <sub>2</sub>          | CO         | HCOO <sup>-</sup> | C <sub>2</sub> H <sub>4</sub> | Ethanol   | Acetate   | Propanol  | Total       | EE <sub>1/2 HCOO<sup>-</sup></sub> |
| <b>Cu-SPy</b>              |                        |                         |            |                   |                               |           |           |           |             |                                    |
| -100                       | -0.33 ± 0.01           | 11.6 ± 4.2              | 8.3 ± 6.7  | 81.4 ± 4.3        | -                             | -         | -         | -         | 101.3 ± 0.5 | 64.9 ± 3.7                         |
| -300                       | -0.41 ± 0.09           | 6.0 ± 1.9               | 21.1 ± 3.1 | 72.4 ± 1.5        | 0.8 ± 0.3                     | 0.2 ± 0.3 | -         | -         | 102.6 ± 1.2 | 55.2 ± 3.2                         |
| -500                       | -0.46 ± 0.06           | 8.1 ± 2.4               | 35.2 ± 4.5 | 41.3 ± 3.5        | 11.8 ± 4.3                    | 1.5 ± 1.0 | 0.3 ± 0.3 | 1.4 ± 0.6 | 99.7 ± 0.6  | 30.7 ± 3.4                         |
| <b>Cu</b>                  |                        |                         |            |                   |                               |           |           |           |             |                                    |
| -100                       | -0.38 ± 0.01           | 12.4 ± 1.5              | 52.8 ± 2.6 | 26.0 ± 2.7        | 10.8 ± 1.7                    | 2.0 ± 0.6 | 0.4 ± 0.1 | 2.5 ± 1.4 | 106.9 ± 0.9 | 20.3 ± 2.2                         |
| -300                       | -0.45 ± 0.04           | 8.2 ± 0.8               | 40.8 ± 3.1 | 21.8 ± 1.5        | 21.0 ± 0.8                    | 4.1 ± 0.7 | 0.6 ± 0.1 | 4.4 ± 0.4 | 100.1 ± 2.4 | 16.3 ± 1.5                         |
| -500                       | -0.53 ± 0.08           | 9.6 ± 1.4               | 29.2 ± 4.0 | 16.8 ± 1.0        | 29.4 ± 2.8                    | 5.9 ± 0.3 | 1.6 ± 0.6 | 5.4 ± 0.6 | 98.2 ± 2.1  | 12.0 ± 1.2                         |

**Table S3** | Cu-SPh, Cu25-SPy, and Cu-DMSPy faradaic efficiencies of main products from CO<sub>2</sub> reduction (1h) at different current densities

| $j / \text{mA cm}^{-2}$ | Faradaic Efficiency / % |            |                   |                               |           |           |           |             |
|-------------------------|-------------------------|------------|-------------------|-------------------------------|-----------|-----------|-----------|-------------|
|                         | H <sub>2</sub>          | CO         | HCOO <sup>-</sup> | C <sub>2</sub> H <sub>4</sub> | Ethanol   | Acetate   | Propanol  | Total       |
| <b>Cu-SPh</b>           |                         |            |                   |                               |           |           |           |             |
| -100                    | 16.0                    | 39.5       | 28.1              | 14.7                          | 1.3       | 0.6       | 0.5       | 100.7       |
| -300                    | 17.0 ± 1.1              | 35.0 ± 1.3 | 25.4 ± 1.5        | 20.6 ± 5.1                    | 2.5 ± 0.8 | 1.0 ± 0.1 | 2.8 ± 0.6 | 100.3 ± 2.8 |
| -500                    | 23.0                    | 13.0       | 17.7              | 34.4                          | 4.4       | 3.0       | 4.8       | 100.5       |
| <b>Cu25-SPy</b>         |                         |            |                   |                               |           |           |           |             |
| -100                    | 15.9                    | 4.5        | 79.9              | 0                             | 0         | 0         | 0         | 100.4       |
| -300                    | 11.3                    | 15.0       | 71.9              | 2.4                           | 1.2       | 0.5       | 1.0       | 103.3       |
| -500                    | 31.1                    | 17.2       | 26.4              | 14.7                          | 3.5       | 1.7       | 1.4       | 95.9        |
| <b>Cu-DMSPy</b>         |                         |            |                   |                               |           |           |           |             |
| -300                    | 13.1                    | 15.8       | 67.9              | 2.1                           | 0.4       | 0.3       | 0.3       | 99.9        |

**Table S4** | Ligand loss post-electrolysis at different current densities alongside the losses from only flow conditions and electrochemical activation.

| Current Density / mA | Time / h | Ligand loss / %        |
|----------------------|----------|------------------------|
| No current, in flow  | 1        | 13.9                   |
| Activation step      | -        | 7.7                    |
|                      |          | combined = 21.6        |
| -300                 | 1        | 3.6 ± 0.2 <sup>1</sup> |
| -300                 | 4        | 3.3 <sup>2</sup>       |
|                      | 6        | 3.3 <sup>2</sup>       |
| -500                 | 0.5      | 21.5                   |
|                      | 1        | 60.7                   |
|                      | 1.5      | 89.8                   |
|                      | 2        | 105.5                  |

<sup>1</sup>Value does not include any losses from flow conditions with no applied potential or activation as the electrode was pre-activated and a fresh solution was used

<sup>2</sup>Accounting for losses through activation and flow conditions without applied potential

**Table S5** | Adsorption energies of COOH, OCOH, and OCOH' on Cu and Cu-SPy

| <b>Catalyst</b> | <b>Species</b> | <b>Adsorption site</b> | <b><math>\Delta E_{ads}</math> (eV)</b> |
|-----------------|----------------|------------------------|---|
| Cu              | COOH           | bridge                 | -2.96                                   |
|                 | OCOH           | bridge                 | -2.26                                   |
|                 | OCOH'          | bridge                 | -2.32                                   |
| Cu-SPy          | COOH           | bridge                 | -3.13                                   |
|                 | OCOH           | bridge                 | -2.00                                   |
|                 | OCOH'          | bridge                 | -2.17                                   |

**Table S6** | Free energy corrections for different species at T = 298.15 K

|                                   | <i>EZPE</i> (eV) | $\int C_{v,i} dT$ (eV) | - <i>TS</i> (eV) |
|-----------------------------------|------------------|------------------------|------------------|
| <b>Reactants and Products</b>     |                  |                        |                  |
| H <sub>2(g)</sub>                 | 0.276            | 0.109                  | -0.528           |
| H <sub>2O</sub> ( <sub>aq</sub> ) | 0.561            | 0.077                  | -0.585           |
| CO <sub>2</sub> ( <sub>aq</sub> ) | 0.314            | 0.112                  | -0.750           |
| CO( <sub>g</sub> )                | 0.145            | 0.102                  | -0.691           |
| HCOOH( <sub>aq</sub> )            | 0.903            | 0.147                  | -0.893           |
| <b>Adsorbed species on Cu</b>     |                  |                        |                  |
| *                                 | 0.000            | 0.000                  | 0.000            |
| *COOH                             | 0.613            | 0.103                  | -0.210           |
| *OCOH                             | 0.600            | 0.111                  | -0.237           |
| *OCOH'                            | 0.598            | 0.106                  | -0.212           |
| *CO                               | 0.160            | 0.087                  | -0.198           |
| <b>Adsorbed species on Cu-SPy</b> |                  |                        |                  |
| *                                 | 2.100            | 0.191                  | -0.382           |
| *COOH                             | 2.733            | 0.290                  | -0.579           |
| *OCOH                             | 2.720            | 0.286                  | -0.570           |
| *OCOH'                            | 2.700            | 0.302                  | -0.619           |
| *CO                               | 2.295            | 0.265                  | -0.531           |

## Supplementary References

1. García de Arquer, F. P. *et al.* CO<sub>2</sub> electrolysis to multicarbon products at activities greater than 1 A cm<sup>-2</sup>. *Science* **367**, 661–666 (2020).
2. Yoakim, C. *et al.* Novel nevirapine-like inhibitors with improved activity against NNRTI-resistant HIV: 8-Heteroarylthiomethyldipyridodiazepinone derivatives. *Bioorganic Med. Chem. Lett.* **14**, 739–742 (2004).
3. Kresse, G. & Hafner, J. Ab initio molecular dynamics for liquid metals. *Phys. Rev. B - Condens. Matter Mater. Phys.* **47**, 558–561 (1993).
4. Kresse, G. & Hafner, J. Ab initio molecular-dynamics simulation of the liquid-metal–amorphous-semiconductor transition in germanium. *Phys. Rev. B - Condens. Matter Mater. Phys.* **49**, 14251–14269 (1994).
5. Kresse, G. & Furthmüller, J. Efficiency of ab-initio total energy calculations for metals and semiconductors using a plane-wave basis set. *Comput. Mater. Sci.* **6**, 15–50 (1996).
6. Kresse, G. & Furthmüller, J. Efficient iterative schemes for ab initio total-energy calculations using a plane-wave basis set. *Phys. Rev. B - Condens. Matter Mater. Phys.* **54**, 11169–11186 (1996).
7. Blöchl, P. E. Projector augmented-wave method. *Phys. Rev. B* **50**, 17953–17979 (1994).
8. Kresse, G. & Joubert, D. From ultrasoft pseudopotentials to the projector augmented-wave method. *Phys. Rev. B - Condens. Matter Mater. Phys.* **59**, 1758–1775 (1999).
9. Grimme, S., Antony, J., Ehrlich, S. & Krieg, H. A consistent and accurate ab initio parametrization of density functional dispersion correction (DFT-D) for the 94 elements H-Pu. *J. Chem. Phys.* **132**, 154104 (2010).
10. Pulay, P. Convergence acceleration of iterative sequences. the case of scf iteration. *Chem. Phys. Lett.* **73**, 393–398 (1980).
11. Goodpaster, J. D., Bell, A. T. & Head-Gordon, M. Identification of Possible Pathways for C-C Bond Formation during Electrochemical Reduction of CO<sub>2</sub>: New Theoretical Insights from an Improved Electrochemical Model. *J. Phys. Chem. Lett.* **7**, 1471–1477 (2016).
12. Garza, A. J., Bell, A. T. & Head-Gordon, M. Mechanism of CO<sub>2</sub> Reduction at Copper Surfaces: Pathways to C<sub>2</sub> Products. *ACS Catal.* **8**, 1490–1499 (2018).
13. Cheng, M. J., Clark, E. L., Pham, H. H., Bell, A. T. & Head-Gordon, M. Quantum Mechanical Screening of Single-Atom Bimetallic Alloys for the Selective Reduction of CO<sub>2</sub> to C<sub>1</sub> Hydrocarbons. *ACS Catal.* **6**, 7769–7777 (2016).
14. Hammer, B., Hansen, L. B. & Nørskov, J. K. Improved adsorption energetics within density-functional theory using revised Perdew-Burke-Ernzerhof functionals. *Phys. Rev. B - Condens. Matter Mater. Phys.* **59**, 7413–7421 (1999).
15. Blaylock, D. W., Tepei Ogura, William, H. G. & Gregory, J. O. B. Computational investigation of thermochemistry and kinetics of steam methane reforming on Ni(111) under realistic conditions. *J. Phys. Chem. C* **113**, 4898–4908 (2009).
16. Peterson, A. A., Abild-Pedersen, F., Studt, F., Rossmeisl, J. & Nørskov, J. K. How copper catalyzes the electroreduction of carbon dioxide into hydrocarbon fuels. *Energy Environ. Sci.* **3**, 1311–1315 (2010).
17. Ma, W. *et al.* Promoting electrocatalytic CO<sub>2</sub> reduction to formate via sulfur-boosting water activation on indium surfaces. *Nat. Commun.* **10**, 1–10 (2019).
18. Jiang, B., Zhang, X. G., Jiang, K., Wu, D. Y. & Cai, W. Bin. Boosting Formate Production in Electrocatalytic CO<sub>2</sub> Reduction over Wide Potential Window on Pd Surfaces. *J. Am. Chem. Soc.* **140**, 2880–2889 (2018).

19. Chadi, D. J. & Cohen, M. L. Special points in the Brillouin zone. *Phys. Rev. B* **8**, 5747–5753 (1973).
20. Makov, G. & Payne, M. C. Periodic boundary conditions in ab initio calculations. *Phys. Rev. B - Condens. Matter Mater. Phys.* **51**, 4014–4022 (1995).
21. Mathew, K., Sundararaman, R., Letchworth-Weaver, K., Arias, T. A. & Hennig, R. G. Implicit solvation model for density-functional study of nanocrystal surfaces and reaction pathways. *J. Chem. Phys.* **140**, 084106 (2014).
22. Mathew, K., Kolluru, V. S. C., Mula, S., Steinmann, S. N. & Hennig, R. G. Implicit self-consistent electrolyte model in plane-wave density-functional theory. *J. Chem. Phys.* **151**, 234101 (2019).
23. Mathew, K., Rhennig & Bértoli, J. Henniggroup/VASPsol: VASPsol Solvation Module V1.0. <https://github.com/henniggroup/VASPsol> (2018) doi:10.5281/ZENODO.2555053.
24. García-Muelas, R. *et al.* Origin of the Selective Electroreduction of Carbon Dioxide to Formate by Chalcogen Modified Copper. *J. Phys. Chem. Lett.* **9**, 7153–7159 (2018).
25. Nørskov, J. K. *et al.* Origin of the overpotential for oxygen reduction at a fuel-cell cathode. *J. Phys. Chem. B* **108**, 17886–17892 (2004).
26. Liang, Q., Brocks, G. & Bieberle-Hütter, A. Oxygen evolution reaction (OER) mechanism under alkaline and acidic conditions. *JPhys Energy* **3**, 026001 (2021).
27. Alfonso, D. R., Tafen, D. N. & Kauffmann, D. R. First-Principles Modeling in Heterogeneous Electrocatalysis. *Catal. 2018, Vol. 8, Page 424* **8**, 424 (2018).
28. Bagger, A., Castelli, I. E., Hansen, M. H. & Rossmeisl, J. Fundamental Atomic Insight in Electrocatalysis. in *Handbook of Materials Modeling* (eds. Andreoni, W. & Yip, S.) 1–31 (Springer, Cham, 2018). doi:10.1007/978-3-319-50257-1\_8-1.
29. Oberhofer, H. Electrocatalysis Beyond the Computational Hydrogen Electrode. in *Handbook of Materials Modeling* (eds. Andreoni, W. & Yip, S.) 1–33 (Springer, Cham, 2018). doi:10.1007/978-3-319-50257-1\_9-1.
30. Singh, P. *et al.* Electrochemical Capture and Release of Carbon Dioxide Using a Disulfide–Thiocarbonate Redox Cycle. *J. Am. Chem. Soc.* **139**, 1033–1036 (2017).
31. Pankhurst, J. R., Iyengar, P., Loiudice, A., Mensi, M. & Buonsanti, R. Metal-ligand bond strength determines the fate of organic ligands on the catalyst surface during the electrochemical CO<sub>2</sub> reduction reaction. *Chem. Sci.* **11**, 9296–9302 (2020).